



Highly active and stable stepped Cu surface for enhanced electrochemical CO₂ reduction to C₂H₄

Chungseok Choi ¹, Soonho Kwon ², Tao Cheng ^{1,3}, Mingjie Xu ^{4,5,6}, Peter Tieu ^{1,7}, Changsoo Lee ^{1,8}, Jin Cai ¹, Hyuck Mo Lee ^{1,8}, Xiaoqing Pan ^{1,4,5,9}, Xiangfeng Duan ^{1,10}, William A. Goddard III ^{1,2} and Yu Huang ¹✉

Electrochemical CO₂ reduction to value-added chemical feedstocks is of considerable interest for renewable energy storage and renewable source generation while mitigating CO₂ emissions from human activity. Copper represents an effective catalyst in reducing CO₂ to hydrocarbons or oxygenates, but it is often plagued by a low product selectivity and limited long-term stability. Here we report that copper nanowires with rich surface steps exhibit a remarkably high Faradaic efficiency for C₂H₄ that can be maintained for over 200 hours. Computational studies reveal that these steps are thermodynamically favoured compared with Cu(100) surface under the operating conditions and the stepped surface favours C2 products by suppressing the C1 pathway and hydrogen production.

Developing highly efficient electrocatalysts for the carbon dioxide reduction reaction (CO₂RR) to value-added fuels and chemicals offers a feasible pathway for renewable energy storage and could help mitigate the ever-increasing carbon dioxide (CO₂) emissions from human activities¹. Several metal electrodes are known to catalyse CO₂RR in aqueous solutions². Among the catalysts explored to date, copper (Cu) is the only electrocatalytic material that converts CO₂ into hydrocarbons or oxygenates products with a significant activity and efficiency³. Additionally, owing to Cu's natural abundance^{4,5} and low cost, it has been intensively studied for CO₂RR for decades^{4,6–13}. However, the low product selectivity towards valuable fuel products and the lack of long-term stability remain major challenges for Cu-based catalysts¹¹. Various approaches have been explored to address these challenges^{6–18}. For example, Kanan and co-workers reported that the grain boundaries on Cu film^{16,17} and surface defects¹⁸ promote the production of hydrocarbons with one-carbon (C1 product)¹³ (~45% CO at −0.5 V and ~33% HCO₂H at −0.65 V versus the reversible hydrogen electrode (RHE), referenced to all potentials in this article unless otherwise specified). Moreover, residual surface copper oxides^{14,19,20} have been suggested to enhance the production of hydrocarbons with two carbons (C2)¹⁴.

Among the major gaseous products, ethylene (C₂H₄) is desirable as it is a basic building block to produce various plastics, solvents and cosmetics. In 2020 alone, 207.4 million tons of C₂H₄ consumption is projected, and the annual demand for C₂H₄ is expected to grow ~4.5% through to 2027²¹. However, the selective production of C₂H₄ from CO₂RR is challenging, with competition from the hydrogen evolution reaction (HER) and methane (CH₄) production²². It has been predicted and shown with single-crystal studies

that the formation of specific surface step sites on Cu catalysts can lower the barrier for CO dimerization to promote C2 production over C1 products^{23,24}. Indeed, Cheng et al. performed a thorough density functional theory (DFT) screening of active defect sites for electrochemical CO₂RR to C2 products at grain boundaries of Cu nanoparticles (NPs)²³. They found that the most active surface sites for C2 production on grain boundaries consist of one strong CO binding site next to one weak CO binding site, which significantly reduces the energy of the *OCCHO transition state and makes it active towards C2 products²³.

Here we report the preparation of Cu nanowires (CuNWs) with highly active stepped surfaces through the *in situ* electrochemical activation of pre-grown CuNWs with {100} surface (Fig. 1). The electrochemical CO₂RR studies demonstrate a remarkably high C2 selectivity with a Faradaic efficiency (FE) towards C₂H₄ (FE_{C₂H₄} > 70%), as well as exceptionally high stability for ~200 hours. The high C₂H₄ selectivity is attributed to the unique surface structure of the CuNWs with abundant stepped sites. Our DFT studies showed that the Cu(511) plane [3(100)×(111)] stepped surface is thermodynamically favoured at CO₂RR conditions over either Cu(100) or Cu(111) under the operating conditions, which explains the experimentally observed long-term stability. The calculations also revealed a higher barrier for the C1 path, along with a slower HER on Cu(511) compared with that of C2, which leads to the greatly enhanced selectivity towards C₂H₄.

Results

Preparation of CuNWs with surface steps. The CuNWs were synthesized with a protocol similar to a previously reported approach²⁵, and the resulting CuNWs typically display a fivefold twin with the

¹Department of Materials Science and Engineering, University of California, Los Angeles, Los Angeles, CA, USA. ²Department of Applied Physics and Materials Science, California Institute of Technology, Pasadena, CA, USA. ³Institute of Functional Nano & Soft Materials (FUNSOM), Jiangsu Key Laboratory for Carbon-Based Functional Materials & Devices, Joint International Research Laboratory of Carbon-Based Functional Materials and Devices, Soochow University, Suzhou, P. R. China. ⁴Irvine Material Research Institute (IMRI), University of California, Irvine, Irvine, CA, USA. ⁵Department of Materials Science and Engineering, University of California, Irvine, Irvine, CA, USA. ⁶Fok Ying Tung Research Institute, The Hong Kong University of Science and Technology, Guangzhou, P. R. China. ⁷Department of Chemistry, University of California, Irvine, Irvine, CA, USA. ⁸Department of Materials Science and Engineering, Korea Advanced Institute of Science and Technology, Yuseong-gu, Republic of Korea. ⁹Department of Physics and Astronomy, University of California, Irvine, Irvine, CA, USA. ¹⁰Department of Chemistry and Biochemistry, University of California, Los Angeles, Los Angeles, CA, USA. ✉e-mail: wag@caltech.edu; yhuang@seas.ucla.edu

ARTICLES

NATURE CATALYSIS

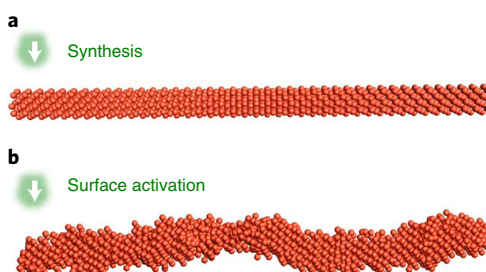


Fig. 1 | Schematic of preparing CuNWs with surface steps. **a**, The as-synthesized CuNWs with a {100} surface. **b**, The CuNWs are activated *in situ* during the electrochemical CO₂RR to form surface steps.

[110] axial direction and {100} side facets (see Methods for details). The synthesized CuNWs (termed Syn-CuNWs) were collected by centrifuge and washed five times with a hexane/ethanol mixture. The structure of the Syn-CuNWs was characterized by powder X-ray diffraction, transmission electron microscopy (TEM) and secondary electron imaging (SEI). The powder X-ray diffraction peaks of Syn-CuNWs match those of Cu (Supplementary Fig. 1a). A low-resolution TEM image of the Syn-CuNWs demonstrates its one-dimensional wire structure with a smooth surface (Fig. 2a) and an average diameter of 25 ± 7.7 nm (Supplementary Fig. 1b). A high-resolution TEM (HRTEM) of the Syn-CuNWs (Fig. 2a inset) shows a 1.27 \AA lattice spacing of Cu{220} and the Cu<110> direction, which is consistent with the expected <110> axial-growth direction of the Syn-CuNWs^{25,26}.

To generate surface steps, the Syn-CuNWs were subjected to electrochemical activation environment similar to that of the CO₂RR, that is under a high reduction bias ($V = -1.05$ V) in 0.1 M KHCO₃ electrolyte solution for over 30 minutes. After this electrochemical activation, the activated CuNWs (termed A-CuNWs) showed highly uneven surfaces (Fig. 2b). HRTEM of A-CuNWs after one hour of activation showed zone [011] of fast Fourier transform (FFT) spots. The plane spacing in zone [011] of the FFT spots shows 2.08 \AA , 1.80 \AA and 1.27 \AA , which indexed as Cu{111}, Cu{200} and Cu{220}, respectively (Fig. 2c,d)^{25,26}. Both the Cu₂O and Cu phases were found on the A-CuNW surface with the <110> axial direction and <100> towards the sides, which suggests a {100}-rich side surface (Fig. 2c and Supplementary Fig. 2). The Cu₂O observed in HRTEM on the surface of the A-CuNWs was probably due to the instant surface oxidation after removing the reduction potential²⁰, which will convert back to Cu under applied reduction potentials of about -0.8 to -1.1 V (ref. ²⁷). The HRTEM images on the A-CuNW surface also indicated the formation of surface steps, with some in the form of $[n(100) \times m(111)]$ (Fig. 2d and Supplementary Fig. 2).

In addition, SEI in the scanning transmission electron microscopy mode also confirmed a pronounced roughened or stepped topology of the A-CuNWs compared with that of the Syn-CuNWs (Supplementary Fig. 3). We further performed lead (Pb) under potential deposition²⁸ (Supplementary Fig. 4), which revealed that the electrochemical surface area (ECSA) of the A-CuNWs ($3.07\text{ m}^2\text{ g}^{-1}$) was higher than that of the Syn-CuNWs ($1.68\text{ m}^2\text{ g}^{-1}$). Thus, the electrochemical surface activation process produced A-CuNWs with stepped surfaces and with an increased ECSA. Moreover, electrochemical impedance spectroscopy showed that the A-CuNWs have a slightly lower ohmic resistance (42 \Omega) than that of the Syn-CuNWs (45 \Omega) (Supplementary Fig. 5).

Electrochemical characterization of CuNW surfaces. To further evaluate the surface features of the CuNWs, we examined OH⁻ adsorption spectra on the catalyst surface through the Cu ↔ Cu₂O

redox reaction cyclic voltammetry (CV) (see Methods for details) (Supplementary Fig. 6). The Syn-CuNWs showed OH⁻ adsorption peaks at 0.362 and 0.395 V (Fig. 3a), which correspond to the Cu(OH) adsorption (Cu(OH)_{ad}) peaks on Cu{100} and Cu{110}, respectively^{29–32}. In particular, the most pronounced Cu(OH)_{ad} peak at 0.362 V corresponds well with the expected Cu{100} facet on the Syn-CuNW surface. Interestingly, compared with Syn-CuNWs, one additional OH⁻ adsorption peak emerged at 0.316 V (Fig. 3a) on A-CuNWs. This additional peak (assigned here to A-(*hkl*)) appeared at a more negative potential than those of the low-index facets of Cu, which indicates a stronger OH⁻ adsorption^{33,34}, which has been assigned to Cu surfaces with high-energy steps^{31,35}. For example, Raciti et al. reported an OH⁻ adsorption peak (~ 0.33 V) with a negative shift from the Cu{100} peak (~ 0.35 V), which they assigned to Cu(211) ($[3(111) \times (100)]$) (ref. ³¹). DFT calculations of Cu–O binding energy by Tian and Wang also reported that the stepped surface of Cu(311) ($[2(100) \times (111)]$) led to a stronger Cu–O binding energy compared with those of Cu(100) and Cu(111) (ref. ³⁵). To gain a more quantitative evaluation of the surface-facet evolution, we estimated the percentage of the surface planes on Syn-CuNWs and A-CuNWs by integrating each OH_{ad} peak after subtracting the background (Fig. 3b–e and Supplementary Fig. 7). The Syn-CuNW surface comprised mostly Cu{100} (67%) and Cu{110} (32%) (Fig. 3b), consistent with a nanowire structure with side facets that are mostly {100} with some {110} (schematic in Fig. 3b). Compared with Syn-CuNWs (Fig. 3b), A-CuNWs showed an increased percentage of A-(*hkl*) with a prolonged activation time from 0% (0 h), 17% (0.5 h), 28% (1 h) to 41% (1.5 h) (Fig. 3f). Meanwhile, Cu{100} and Cu{110} reduced from 67% to 39% and from 32% to 19%, respectively (Fig. 3f and Supplementary Table 1). These observations suggest that the {100} and {110} expressed on the Syn-CuNW surface gradually transformed into the higher-energy A-(*hkl*) surface structures during the electrochemical activation process, which is consistent with the TEM observations (Fig. 2).

Electrochemical CO₂RR evaluation. We studied the CO₂RR performance of CuNW catalysts with a gas-tight H cell by analysing the effluent gas and liquid products at different applied potentials between -0.75 and -1.1 V in CO₂-saturated 0.1 M KHCO₃ (pH 6.8) at room temperature and under atmospheric pressure. The current density (*j*) and ECSA of the CuNWs were evaluated using the rotating disk electrode, the CO₂RR performances were evaluated in the H cell coupled with gas chromatography barrier ionization discharge (GC-BID) (see the Methods for details). The performance of the A-CuNW catalysts was compared with those of commercial Cu foil and Syn-CuNWs (Fig. 4a–c). As most of the products from CO₂RR on our catalysts were in the gas phase, we focus our discussions of the CO₂RR performances on gas-phase products (Supplementary Tables 2–4). First, we observed that the A-CuNWs (with one hour activation) showed a considerably higher yield of C₂H₄ with an average peak FE_{C₂H₄} of $69.79 \pm 1.44\%$ at around -1.00 V (Fig. 4c and Supplementary Table 2), when compared with the Syn-CuNWs (FE_{C₂H₄} = $44.65 \pm 2.20\%$) (Fig. 4b and Supplementary Table 3) and the polycrystalline Cu foil (FE_{C₂H₄} = $22.80 \pm 4.60\%$). We note that the primary CO₂RR products of the polycrystalline Cu foil were found to be CH₄ ($24.67 \pm 5.15\%$) and C₂H₄ ($22.80 \pm 4.60\%$) around -1 V (Supplementary Table 4), which is consistent with a previously reported CO₂RR of Cu polycrystalline foil³⁶.

Overall, compared with Syn-CuNWs, the A-CuNWs showed a higher partial current density of FE_{C₂H₄} and a much lower HER partial current density (Supplementary Fig. 9). It has been reported that a high surface roughness could lead to enhanced C₂H₄ production¹², we further compared the FE_{C₂H₄} between commercial 25 nm Cu NPs and the A-CuNWs. We found that A-CuNWs showed less surface roughness, but still exhibited a FE_{C₂H₄} about 30% higher

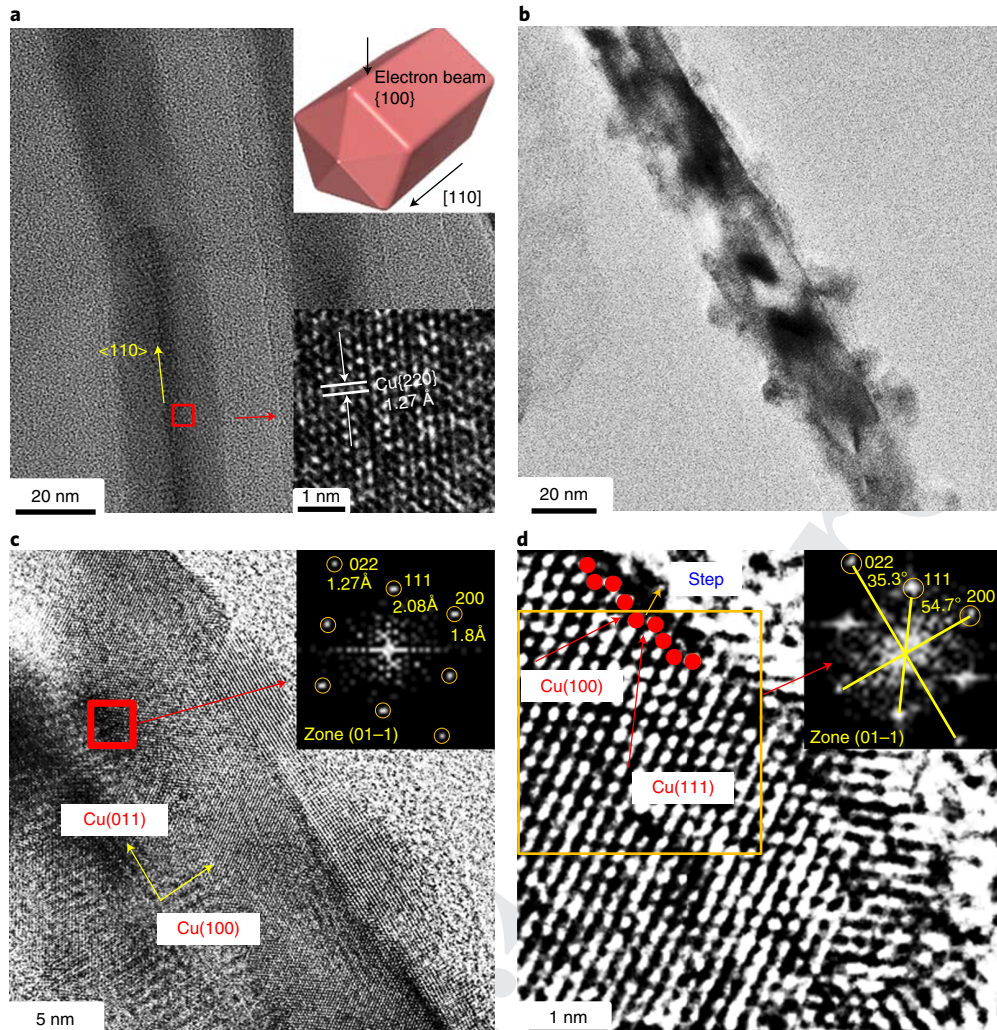


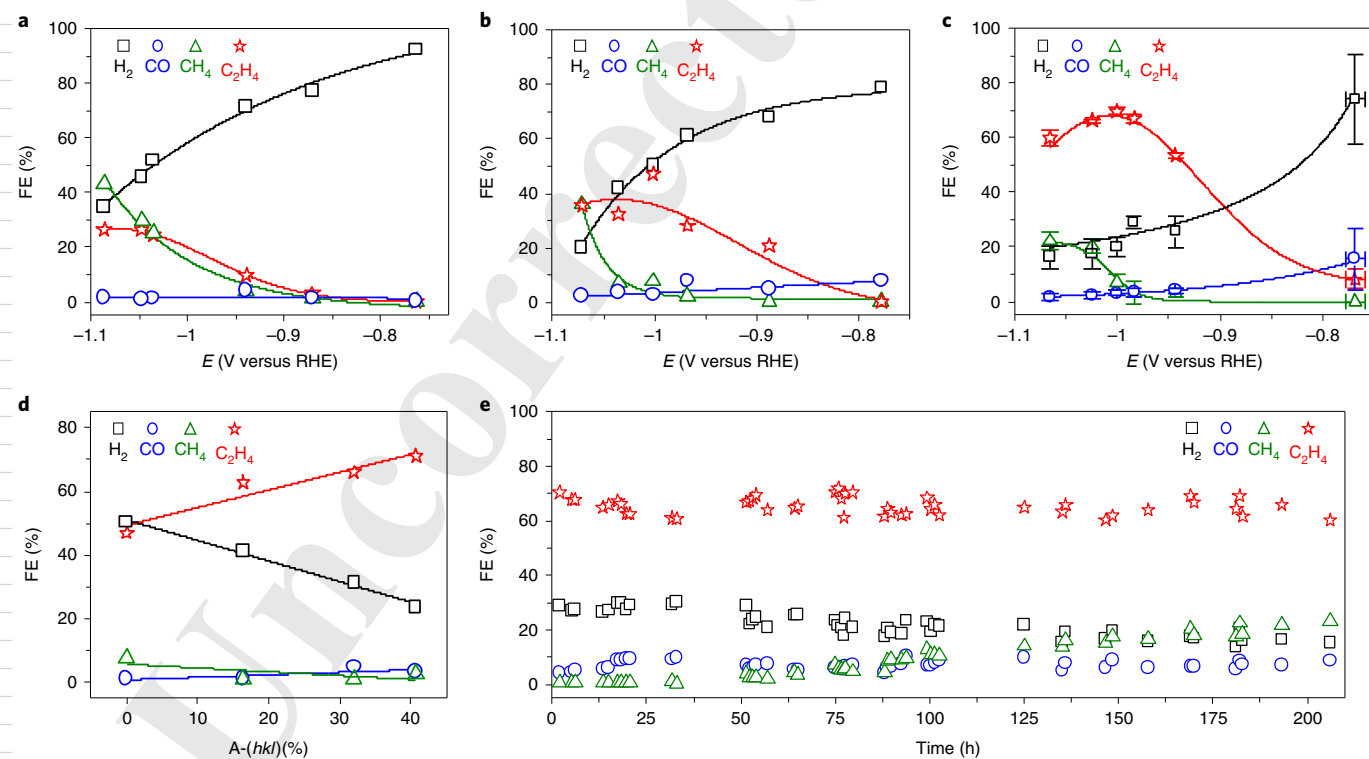
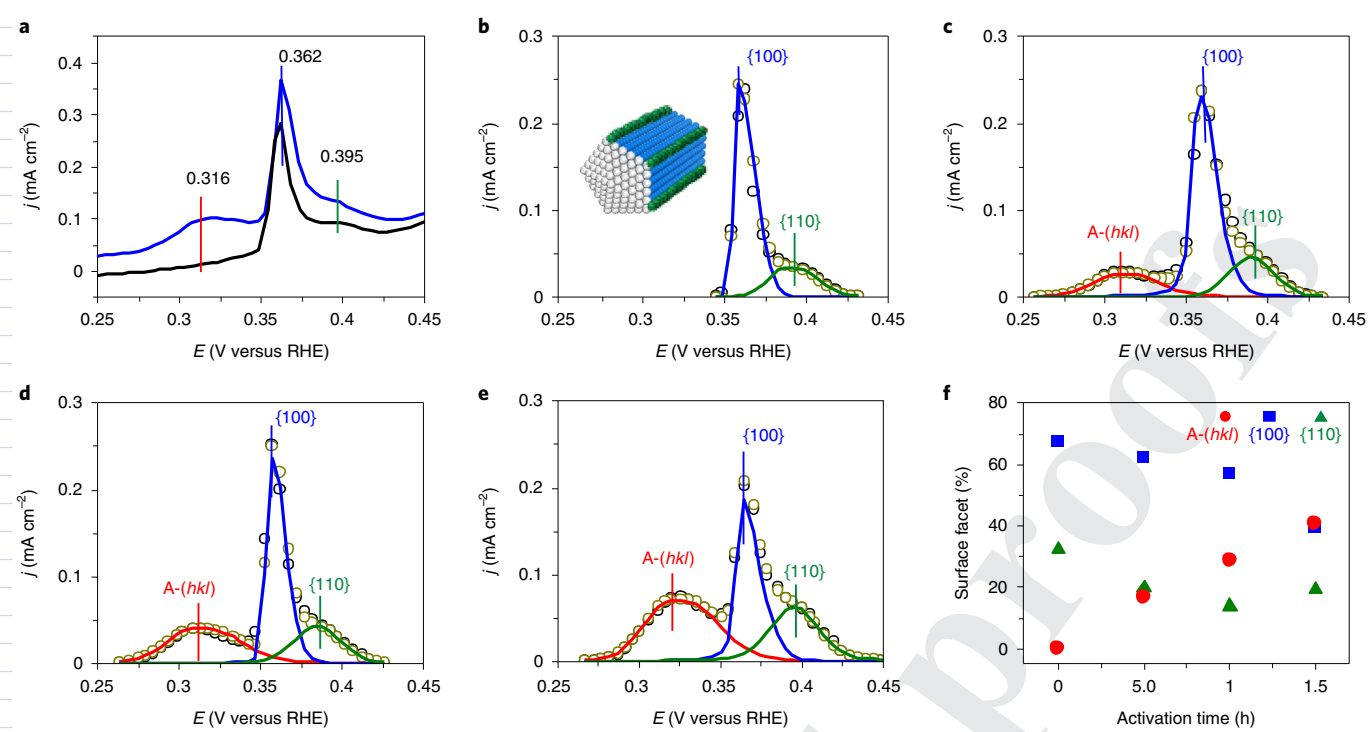
Fig. 2 | TEM characterizations of the Syn-CuNW and A-CuNW. **a**, Low magnification TEM image of Syn-CuNWs. Insets: schematic illustration (top) and HRTEM (bottom) of a Syn-CuNW showing the electron beam direction, [110] nanowire axial growth direction and expressed {100} side facets. **b**, Low-magnification TEM image of A-CuNW. **c**, HRTEM image of A-CuNW. Inset: FFT of the corresponding Cu phase, which indicates the [110] axial direction and expression of the {100} planes on the side surface. **d**, HRTEM image of an A-CuNW surface indicating the step structure. Inset: FFT from yellow box).

than that of the commercial 25 nm Cu NPs ($37.08 \pm 6.87\%$ FE_{C₂H₄} at -1.00 ± 0.01 V) (Supplementary Fig. 10), which rules out the likely contribution from a sample surface roughness to product selectivity. Hence, we tentatively attribute the high C₂H₄ selectivity observed in A-CuNWs to their highly stepped surface.

To further confirm the correlation of FE_{C₂H₄} with the stepped-surface structure A-(*hkl*), we further compared different products from A-CuNWs with different activation durations and thus different surface portions of A-(*hkl*). Significantly, a clear correlation was observed between FE_{C₂H₄} and the value of A-(*hkl*). Specifically, as the stepped surface A-(*hkl*) gradually increased from 0 to 40.68%, the FE_{C₂H₄} correspondingly increased from 47.04 to 71.19% (Fig. 4d). At the same time, we observed decreasing FE_{CH₄} and FE_{H₂} values with increasing A-(*hkl*) (Fig. 4d).

Importantly, these A-CuNWs with stepped surfaces exhibited a sustained high CO₂RR performance during the stability test. The A-CuNWs showed stable C₂H₄ production (61–72% FE_{C₂H₄}) for 205 hours at the corrected potentials ranging from -0.97 to -1.07 V (Fig. 4e). In comparison, the Cu foil only showed stability for less than two hours with ~ 20 –34% FE_{CH₄} at -1.07 V (Supplementary Fig. 11). A repeated stability test that lasted 198 hours further confirmed the

sustainable high performance of A-CuNWs with 64%–79% FE_{C₂H₄} (Supplementary Fig. 12). The sustained high FE_{C₂H₄} suggested a high stability of the A-(*hkl*) surface steps on A-CuNWs. Indeed, the OH_{ad} spectra of A-CuNWs showed that the A-(*hkl*) portion remained at a stable range within $45.40 \pm 5.62\%$ for ~ 200 hours after the initial activation period (~ 1.5 hours) (Supplementary Fig. 13a). We also observed that during the stability test, the A-(*hkl*) continued to increase slightly with the ongoing CO₂RR after the initial 1.5 hours of activation (Supplementary Fig. 13b,c), correspondingly led to a further increase in FE_{C₂H₄} (Supplementary Fig. 13d). The highest FE_{C₂H₄} (79%) was hence achieved around 24 hours into the reaction during the stability test, which corresponds to an A-(*hkl*) of around 50% (Supplementary Figs. 12 and 13). Over 16 stability tests at a potential of around -1 V, we obtained a remarkably high FE_{C₂H₄} of $\sim 77.40 \pm 3.16\%$ (Table 1). Additionally, the SEI images confirmed that the A-CuNWs retained their one-dimensional morphology and stepped surface topology after the long-term stability tests (Supplementary Fig. 14). Together, the A-CuNWs demonstrated a remarkably high FE_{C₂H₄} while maintaining their exceptional stability for 200 hours of continuous operation in a H-cell (Table 1 and Supplementary Table 5).



Catalysts	Applied potentials (V versus RHE)	$J_{C_2H_4}$ (mA cm ⁻²)	Maximum FE _{C₂H₄} (%)	Electrolyte	CO ₂ flow rate (sccm)	Reference
A-CuNWs	-1.01±0.01	~17.3	77.40±3.16	0.1M KHCO ₃	15	This work
Cu nanocube (250–300 nm)	-0.95	11.2	45	0.1M KHCO ₃	20	54
Cu nanocube (10–40 nm)	~-0.86	6.7	33	0.1M KHCO ₃	20	55
Plasma-treated Cu foil	-0.90	7.2	60	0.1M KHCO ₃	30	14
Electro-redesposited Cu	-1.20	22.2	39	0.1M KHCO ₃	20	56
Branched CuO NPs	-1.05	~17.0	~70	0.1M KHCO ₃	60	57
Cu-based NPs	-1.10	~10.0	57	0.1M KHCO ₃	20	58

The FE_{C₂H₄} of A-CuNWs is the average from 16 measurements in the stability tests.

DFT studies of surface stability and activity. The observation of a long-term stability of the high-index A-(*hkl*) surface is rather counterintuitive and intriguing, as high-energy surface steps were generally believed to be less stable than the low-index ones. To this end, we sought to assess the stability of the stepped surface under the working conditions. We performed grand canonical DFT calculations based on the Cu(S) [*n*(100)×*m*(111)] stepped surface to construct the surface phase diagram. Figure 5a,b shows the surface energies for Cu(100), Cu(111) and Cu(511) ([3(100)×(111)]) as a function of RHE potential. On Cu(100), we found one monolayer (ML) of hydrogen (H) for $U < -0.07$ V and 2ML H for $U < -0.83$ V for equilibrium H coverage (θ_H). On Cu(511), we found 1ML H for $U < -0.10$ V, 1.33 ML H for $U < -0.74$ V and that a further increase of H* evokes a severe surface reconstruction. On Cu(111), 1ML H ($U < -0.08$ V) is the maximum coverage, which allows a local minimum of H* without any imaginary frequency. At $U = -0.98$ to -1.06 V, Cu(511) with $\theta_H = 1.33$ has the lowest surface energy compared with Cu(100) at $\theta_H = 2$ and Cu(111) at $\theta_H = 1$ in (Fig. 5a,b). Therefore, we expect that once the stepped surface is formed, there is no driving force to reconstruct back to the flat Cu(100) surface at the working potential, which provides a good stability for the stepped surfaces.

We also calculated CO adsorption free energies to verify if the stepped surface is beneficial for CO adsorption, as the CO population is a key factor for C₂+ products. We found that the step on Cu(511) leads to a 0.17 eV higher affinity for a single CO adsorption compared with that of Cu(100), as shown in Table 2. Moreover, the two adjacent molecular CO adsorptions can occur cooperatively, which is 0.44 eV more stable on the step sites on Cu(511) compared with those on Cu(100), where the c(2×2)-CO adlayer structure was observed in an operando STM study³⁷. Therefore, we confirmed that the step on Cu(511) can secure a higher local CO surface population, and that this facet is also favourable for two adjacent CO adsorptions, which is beneficial for C–C coupling.

Next, we performed DFT to explain the reaction kinetics. The OCCHO* intermediate is an important intermediate towards the production of C₂ products, especially at higher overpotentials^{38,39}, whereas the HCO* intermediate can branch out to form either HCOH* for the C1 pathway or OCCHO* for the C2 pathway. We calculated the reaction energy barriers (ΔG^\ddagger) and reaction free energies (ΔG) for each pathway, as shown in Table 2. The frequency contributions are listed in Supplementary Table 6. To calculate the kinetic barrier for the protonation of the HCO* intermediate into HCOH*, we introduced a surface water molecule as a proton source at pH 6.8. The reduction of HCO* to HCOH* occurs with $\Delta G^\ddagger = 0.53$ eV on Cu(100) and $\Delta G^\ddagger = 0.59$ eV on Cu(511), respectively. Therefore, Cu(511) has a 0.06 eV higher reaction barrier from HCO* to HCOH*, which makes it about ten times slower than that on Cu(100) at 298 K. However, despite the high stability of the 2CO* configuration, the kinetic barrier for C–C coupling from

CO* + HCO* towards OCCHO* (C2 pathway) on Cu(511) is only 0.02 eV higher than that on Cu(100), which makes it only two times slower than that on Cu(100). We also performed DFT calculations for the hydrogen binding energy (HBE) on Cu(100) and on various adsorption sites on Cu(511) to estimate the HER activity based on the fact that a low HER activity for Cu has been attributed to its weak HBE⁴⁰. Compared with the HBE of -0.31 eV on Cu(100), Cu(511) showed even smaller HBEs that ranged from -0.06 to -0.29 eV on various binding sites (Supplementary Fig. 15), which indicates the suppression of HER on Cu(511).

Thus, we suggest that the high local population of 2CO*, the higher barrier for the C1 path on Cu(511) and the slower HER are the key factors that underlie the enhancement in C₂ production observed on A-CuNWs. These results are all consistent with the experimental observations that an increasing surface ratio of the stepped surface A-(*hkl*) led to an increase FE_{C₂H₄}, and decrease in both FE_{CH₄} and FE_{H₂} (Fig. 4d and Supplementary Fig. 13b,c). In addition, the stronger OH⁻ adsorption on A-CuNWs can also induce longer H₂O adsorption residence times on the surface of Cu, which leads to the preference of hydrocarbon products (for example, C₂H₄) over alcohol products (for example, ethanol), which share a common intermediate with C₂H₄ (refs. ^{41,42}). This is consistent with the observed low ethanol production for A-CuNW catalysts (Supplementary Table 2).

Discussion

In conclusion, we report here that CuNW catalysts with a highly stepped surface exhibit a high FE_{C₂H₄} (77.40±3.16%) that is stable for ~200 hours in H-cells. Coupled with structural and electrochemical surface characterizations of A-CuNWs, our DFT calculations showed that the stepped surface [3(100)×(111)] exhibits a high local population of 2CO* and a higher barrier for the C1 path compared with that for Cu(100), which leads to a higher product selectivity towards C₂H₄. These findings suggest an effective approach to engineer catalyst surfaces for high reactivity, high selectivity and high stability under operando conditions.

Methods

Chemicals. Copper(II) chloride dihydrate (CuCl₂·2H₂O, 99.999%), D-(+)-glucose (>99.5%), hexadecylamine (>98%), ethanol (200 proof) and 25 nm Cu NPs were all purchased from Sigma-Aldrich. KOH and hexane (99.9%) were purchased from Fisher Chemical. All the chemicals were used without purification. An ultrapure purification system (Milli-Q advantage A10) produced the deionized water (18.2 MΩ·cm) used to make the solutions. The 99.9% Cu foil obtained from Metal Remnants, Inc. was cut to 1 cm² and mechanically polished by 400G sandpaper from 3M and electrochemically polished in 85% phosphoric acid under -1 V (RHE) for 5 min. The Cu foil was subsequently rinsed with deionized water and used for CO₂RR.

Preparation of CuNW catalysts. In a typical synthesis of the CuNW catalysts, 22 mg of CuCl₂·2H₂O, 50 mg of D-(+)-glucose and 180 mg of hexadecylamine were predissolved in 10 ml of deionized water in a 30 ml vial. The chemical solution

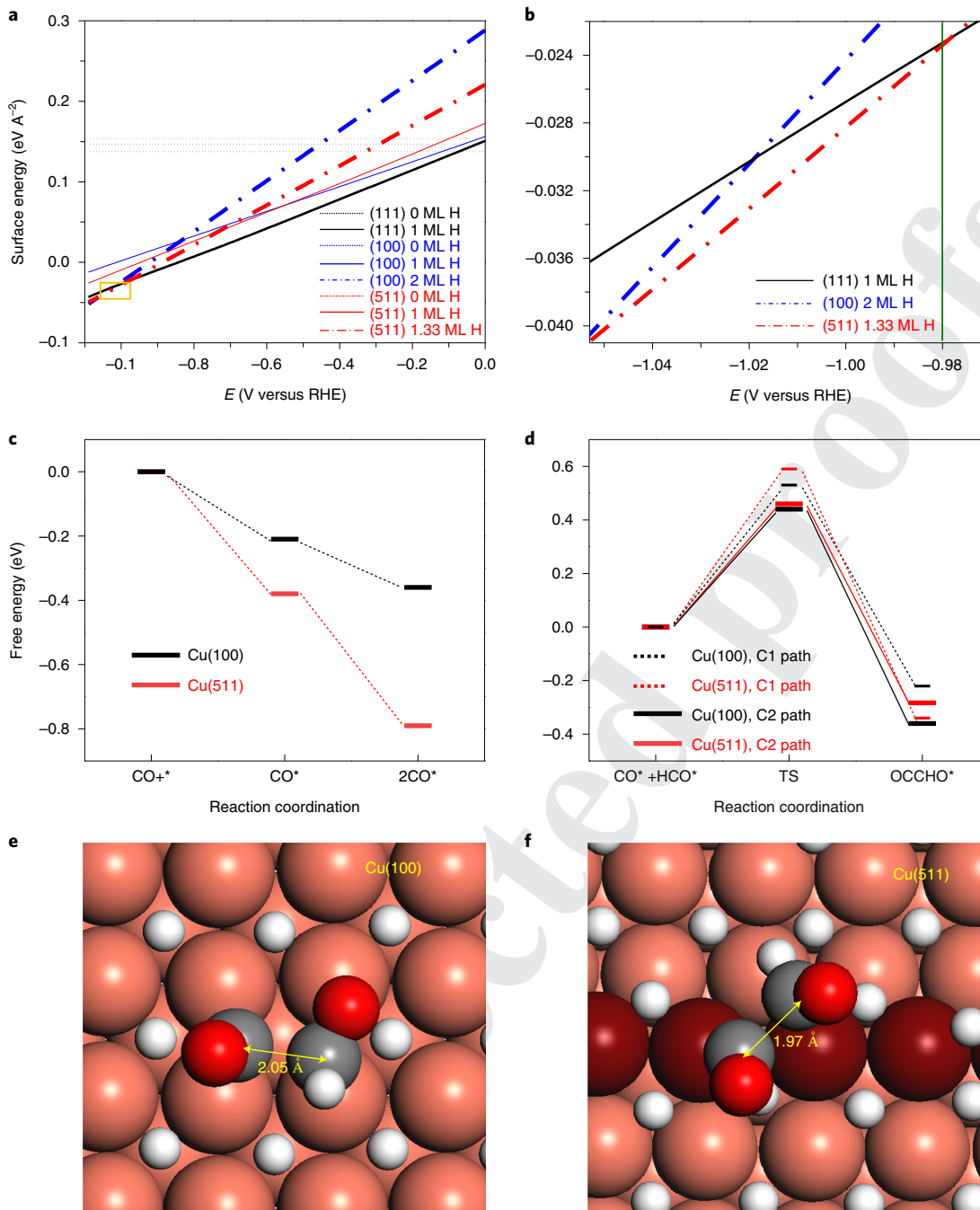


Fig. 5 | The stability and activity of the Cu(511) step surface. **a**, Surface phase diagram of Cu(100) and Cu(511) ([3(100)×(111)]) for 0 ML, 1ML H and the highest stabilized H coverages as a function of potentials at pH 7. **b**, Magnified view of the yellow box in **a**. **c**, CO and 2CO adsorption energies (ΔG_{ads}) on Cu(100) and Cu(511). **d**, C1 and C2 pathways on Cu(100) and Cu(511). **e,f**, Transition states (TS) for the C2 pathway on Cu(100) (**e**) and Cu(511) (**f**). Orange, Cu; grey, C; red, O; white, H.

was mixed under sonication for 15 min and then transferred to an oil bath. The mixture was heated from room temperature to 100°C for 8 h and cooled to room temperature. The Syn-CuNWs were washed five times with sonication in a hexane/ethanol (1:1 volume) solvent for 20 min. The CuNWs were collected by centrifuge at 9,500 rpm.

Characterization of materials. A hexane dispersion of the catalysts was dropped onto and dried on carbon-coated copper TEM grids (Ted Pella) at room temperature to prepare the TEM samples. A FEI CM120 TEM at 120 kV was used for low-resolution TEM images. A FEI Titan TEM operating at 300 kV was used to take the HRTEM images. Dark-field scanning transmission electron microscopy images were taken by a JEM-ARM300F Grand ARM TEM at 300 kV. Scanning

electron microscopy (SEM) images were taken by Nova Nano 230, and SEI was taken by JEOL 2800 TEM with 200 kV. The size of the CuNWs was measured by the largest diameter within the CuNWs. The size was determined by averaging more than 100 nanowires. A Panalytical X'Pert Pro X-ray powder diffractometer with Cu K α radiation was used for the powder X-ray diffraction patterns. Inductively coupled plasma atomic emission spectroscopy (TJA RADIAL IRIS 1000) was conducted to determine the metal concentration in the catalysts used.

Electrode preparation and collecting data for the calculation of FE. Dried CuNWs (4 mg) was mixed with 1 ml of ethanol followed by ultrasonication for 1 h. Subsequently, 10 μ l of Nafion (5 wt%) was added and ultrasonication continued for an extra 10 min. The catalyst ink (10 μ l) of was dropped onto the electrodes

Table 2 | CO ΔG_{ads} , ΔG^\ddagger and ΔG for C1 and C2 pathways by 1ML of H*

1CO*	2CO*	HCO* → HCOH*	CO* + HCO* → OCCHO*		
ΔG_{ads} (eV)	ΔG_{ads} (eV)	ΔG^\ddagger (eV)	ΔG (eV)	ΔG^\ddagger (eV)	ΔG (eV)
Cu(100)	-0.21	-0.36	0.53	-0.22	0.44
Cu(511)	-0.38	-0.80	0.59	-0.34	0.46

using a pipette and dried under ambient air. The 10 µl of the catalysts ink contained 0.04 mg of Cu, which was measured by Inductively coupled plasma atomic emission spectroscopy.

To activate the CuNW catalysts and measure FE, a gas-tight electrolysis H-cell (WizMac) separated with a Nafion ion exchange membrane (Sigma Aldrich) was used. The working electrode coated with catalysts was an L-type glassy-carbon electrode (diameter, 5 mm; area, 0.196 cm²) from WizMac. A Pt coil from Pine Instruments was used as a counter electrode. A 4 M KCl Ag/AgCl electrode from Pine Instruments was used as a reference electrode. The impedance of each solution was tested on a Princeton VersaSTAT 4 electrochemistry workstation. After iR correction, all the discussed potentials were converted into those against RHE.

A 0.1 M KHCO₃ electrolyte solution was used for every electrochemical CO₂RR. Before CO₂RR, we bubbled CO₂ (Airgas, 99.99%) for 30 min to reach saturation, and we kept purging CO₂ into the cathodic compartment at 15 sccm stirring with a stir bar (1,200 r.p.m.) during the CO₂RR. The activation of the CuNW catalysts was conducted with chronoamperometry in a CO₂-saturated 0.1 M KHCO₃ solution at -1.05 V (RHE) for 1 h. We measured the FE by using chronoamperometry for 30–40 min at each applied potential except for the Syn-CuNW catalysts. The FEs of Syn-CuNW catalysts were measured in 10 min to prevent any activation of the CuNW catalysts (Supplementary Fig. 7). For the long-term stability test, the CO₂-saturated 0.1 M KHCO₃ electrolyte was replaced every 12 h and applied pulse potentials (about -0.97 V (RHE) for 600 s and 0.32 V (RHE) for 10 s) to remove possible surface poisoning from the produced formate^{3,44}. The FEs were measured roughly every 2–3 h during the stability test, except for during the night shift. The stability test was performed at room temperature and under atmospheric pressure⁴⁵.

Gas product analysis was done with a Shimadzu Tracera GC-BID 2010 Plus (Shimadzu) equipped with a Restek Micropacked GC column. The standard curve of the GC-BID was calibrated with five standard gases (Airgas). The carrier gas was helium (Airgas, 99.9999%). A p-type Hastelloy six port sampling loop (1.5 ml) was directly routed to an outlet gas line of a gas-tight H-cell. The effluence gas (1.5 ml) was analysed with the Shimadzu Tracera GC-BID 2010 Plus. The FE was calculated as⁴⁶:

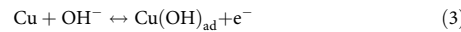
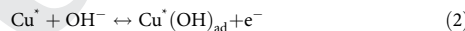
$$\text{FE}_j = \frac{2Fv_jGp_0}{RT_0i_{\text{total}}} \times 100\% \quad (1)$$

where v_j (vol%) is the volume concentration of gas products in the effluence gas from the electrochemical cell (gas chromatography data), G (ml min⁻¹ at room temperature and ambient pressure) is the gas flow rate measured by a ProFlow 6000 electronic flow meter (Restek) at the exit of the electrochemical cell, i_{total} (mA) is the steady-state cell current, $p_0 = 1.01 \times 10^5$ Pa, $T_0 = 298.15$ K, $F = 96,485$ C mol⁻¹ and $R = 8.314$ J mol⁻¹ K⁻¹.

Quantitative NMR spectroscopy (Bruker AV-600) was conducted to analyse the liquid product. Specifically, 0.3 ml of D₂O was added to 0.65 ml of the reacted electrolyte, and 50 µl of dimethyl sulfoxide (0.512 µM ml⁻¹) was also mixed as an internal standard. The one-dimensional ¹H spectrum was measured with a prewater saturation method.

Electrochemical measurements. Before we carried out OH_{ad} on CuNWs, the CuNWs on the L-type glassy-carbon electrode were activated in a H-cell with CO₂-saturated 0.1 M KHCO₃ by purging CO₂ gas. Then, the catalysts on the L-type glassy-carbon electrode were transferred to a three-electrode cell.

For the OH_{ad} adsorption reaction, we conducted OH_{ad} adsorption reaction CV in 0.1 M KOH at a 100 mV s⁻¹ scan rate with Hg/HgO as the reference electrode (CH Instruments). The OH_{ad} adsorption reaction is described accurately by one electron process as follows³³:



To calculate the number of OH_{ad} adsorptions on each Cu plane on the CV scan, the linear background was subtracted³⁰. We integrated currents that correspond to

the assigned Cu{100}, Cu{110} and Cu{111} facets and A-(*hkl*) by each peak scan time as follows:

$$\frac{\int IdV}{v \times e} = \text{the number of OH adsorptions on Cu facets} \quad (4)$$

where I (C s⁻¹) is the current under the OH⁻ absorption peak that corresponds to each Cu facet, dV (V) is the voltage of each Cu facet, v (V s⁻¹) is the scan rate of the OH⁻ adsorption CV scan and e is the electric charge (1.602×10^{-19} C).

For the total current densities and ECSA measurements, a three-electrode cell was used. The working electrode was a glassy-carbon rotating disk electrode (diameter, 5 mm; area, 0.196 cm²) from Pine Instruments and coated with catalysts. A graphite rod was used as the counter electrode. The double junction Ag/AgCl (the inner filling 4 M KCl and the outer filling 10% KNO₃) electrode from Pine Instruments was the reference electrode. The total current densities were measured from CV scans between 0 V and -1.1 V (RHE) at 50 mV s⁻¹ with a rotating disk electrode at 1,200 r.p.m. in CO₂-saturated 0.1 M KHCO₃. Subsequently, ECSAs of the CuNWs were measured by Pb under a potential deposition. The background current was measured in N₂-saturated 0.1 M HClO₄ between 0.26 V and -0.38 V (RHE) at 10 mV s⁻¹. In a N₂-saturated 0.1 M HClO₄ + 0.001 M Pb(ClO₄)₂ solution at room temperature, ECSA measurements were carried out by subtracting the background current from the integrated Pb desorption charge on the CV between 0.26 V and -0.38 V (RHE) at 10 mV s⁻¹ (refs. ²⁸). A conversion factor of 310 µC cm⁻² was based on a monolayer of Pb adatom coverage over Cu and 2e⁻ Pb oxidation²⁸.

Computational details for Cu(100) and Cu(511). The quantum mechanics calculations were carried out using the VASP software version 5.4.4^{46–48} with the Perdew–Burke–Ernzerhof flavour⁴⁹ of DFT. The projector augmented wave method⁵⁰ was used to account for core–valence interactions. The kinetic energy cutoff for plane-wave expansions was set to 500 eV, and reciprocal space was sampled by the Monkhorst–Pack scheme with a grid of $3 \times 3 \times 1$ and $2 \times 3 \times 1$ for Cu(100) and Cu(511), respectively. The vacuum layer was at least 20 Å above the surface. The convergence criteria were 1×10^{-5} eV energy differences to solve the electronic wave function. Methfessel–Paxton smearing of second order with a width of 0.1 eV was applied. All the geometries (atomic coordinates) were converged to within 0.03 eV Å⁻¹ for the maximal components of forces. A poststage vdW DFT-D3 method with Becke–Jónson damping was applied⁵¹. The solvation was treated implicitly using the VASPsol⁵² method.

We employed climbing image nudged elastic band method⁵³ with five images to find the potential energy surface along with the reaction coordinates, and the subsequent dimer method was applied near the saddle point to find the transition state until the force converges to <0.01 eV Å⁻¹. All the transition states had only one imaginary frequency.

All Gibbs free energy (G) values include the vibrational contributions of zero-point vibrational energy (E_{ZPE}), enthalpy (H) and entropy (S). To compare all the surfaces, we normalized the Gibbs free energy to its surface area. The Gibbs free energies were calculated at 298 K and 1 atm, as in:

$$G = H - T\Delta S = E_{\text{DFT}} + E_{\text{ZPE}} + E_{\text{solv}} + \int_0^{298} C_v dT - T\Delta S \quad (5)$$

where E_{DFT} is the DFT-optimized total energy, E_{solv} is the solvation energy, $\int_0^{298} C_v dT$ is the heat capacity and T is the temperature.

For the surface phase diagram, the Gibbs free energy change was calculated at 298 K, pH 7, as in:

$$\Delta G_{\text{surf}} = G_{\text{surf-sol}} - G_{\text{bulk-sol}} - NG_{\text{H}_2\text{O-sol}} + n\left(\frac{1}{2}G_{\text{H}_2}^\circ + k_B T \ln a_{\text{H}^+} - eU\right) \quad (6)$$

where k_B is the Boltzmann constant, a_{H^+} is the proton activity and U is the applied potential.

Structures. The atomic coordinates of the optimized computational models are all provided as a text file in Supplementary Data 1.

Data availability

The data that support the findings of this study are available from the corresponding authors upon reasonable request.

Received: 8 July 2019; Accepted: 30 July 2020;

References

1. Schreier, M. et al. Solar conversion of CO₂ to CO using Earth-abundant electrocatalysts prepared by atomic layer modification of CuO. *Nat. Energy* **2**, 17087 (2017).
2. Hori, Y., Wakebe, H., Tsukamoto, T. & Koga, O. Electrocatalytic process of CO selectivity in electrochemical reduction of CO₂ at metal electrodes in aqueous media. *Electrochim. Acta* **39**, 1833–1839 (1994).

ARTICLES

NATURE CATALYSIS

- 460 3. Hori, Y., Kikuchi, K. & Suzuki, S. Production of CO and CH₄ in
461 electrochemical reduction of CO₂ at metal electrodes in aqueous hydrogen
462 carbonate solution. *Chem. Lett.* **14**, 1695–1698 (1985).
- 463 4. Qiao, J., Liu, Y., Hong, F. & Zhang, J. A review of catalysts for the
464 electro-reduction of carbon dioxide to produce low-carbon fuels. *Chem. Soc.
Rev.* **43**, 631–675 (2014).
- 465 5. Gawande, M. B. et al. Cu and Cu-based nanoparticles: synthesis and
466 applications in catalysis. *Chem. Rev.* **116**, 3722–3811 (2016).
- 467 6. Kim, D., Resasco, J., Yu, Y., Asiri, A. M. & Yang, P. Synergistic geometric and
468 electronic effects for electrochemical reduction of carbon dioxide using
469 gold–copper bimetallic nanoparticles. *Nat. Commun.* **5**, 4948 (2014).
- 470 7. Lu, Q. et al. A selective and efficient electrocatalyst for carbon dioxide
471 reduction. *Nat. Commun.* **5**, 3242 (2014).
- 472 8. Mistry, H., Varela, A. S., Kühl, S., Strasser, P. & Cuenya, B. R. Nanostructured
473 electrocatalysts with tunable activity and selectivity. *Nat. Rev. Mater.* **1**,
474 16009 (2016).
- 475 9. Angamuthu, R., Byers, P., Lutz, M., Spek, A. L. & Bouwman, E.
476 Electrocatalytic CO₂ conversion to oxalate by a copper complex. *Science* **327**,
477 313–315 (2010).
- 478 10. Li, Y. et al. Structure-sensitive CO₂ electroreduction to hydrocarbons on
479 ultrathin 5-fold twinned copper nanowires. *Nano Lett.* **17**, 1312–1317 (2017).
- 480 11. Cheng, T., Xiao, H. & Goddard, W. A. III Reaction mechanisms for the
481 electrochemical reduction of CO₂ to CO and formate on the Cu(100) surface
482 at 298 K from quantum mechanics free energy calculations with explicit
483 water. *J. Am. Chem. Soc.* **138**, 13802–13805 (2016).
- 484 12. Raciti, D., Mao, M., Park, J. H. & Wang, C. Local pH effect in the CO₂
485 reduction reaction on high-surface-area copper electrocatalysts.
J. Electrochem. Soc. **165**, E799 (2018).
- 486 13. Li, C. W. & Kanan, M. W. CO₂ reduction at low overpotential on Cu
487 electrodes resulting from the reduction of thick Cu₂O films. *J. Am. Chem.
Soc.* **134**, 7231–7234 (2012).
- 488 14. Mistry, H. et al. Highly selective plasma-activated copper catalysts for carbon
489 dioxide reduction to ethylene. *Nat. Commun.* **7**, 12123 (2016).
- 490 15. Choi, C. et al. A highly active star decahedron Cu nanocatalyst for
491 hydrocarbon production at low overpotentials. *Adv. Mater.* **31**, 1805405
(2019).
- 492 16. Feng, X., Jiang, K., Fan, S. & Kanan, M. W. Grain-boundary-dependent CO₂
493 electroreduction activity. *J. Am. Chem. Soc.* **137**, 4606–4609 (2015).
- 494 17. Li, C. W., Ciston, J. & Kanan, M. W. Electroreduction of carbon monoxide to
495 liquid fuel on oxide-derived nanocrystalline copper. *Nature* **508**, 504–507
(2014).
- 496 18. Mariano, R. G., McKelvey, K., White, H. S. & Kanan, M. W. Selective increase
497 in CO₂ electroreduction activity at grain-boundary surface terminations.
Science **358**, 1187–1192 (2017).
- 498 19. Favaro, M. et al. Subsurface oxide plays a critical role in CO₂ activation by
499 Cu(111) surfaces to form chemisorbed CO₂, the first step in reduction of
CO₂. *Proc. Natl Acad. Sci. USA* <https://doi.org/10.1073/pnas.1701405114>
(2017).
- 500 20. Lum, Y. & Ager, J. W. Stability of residual oxides in oxide-derived copper
501 catalysts for electrochemical CO₂ reduction investigated with ¹⁸O labeling.
Angew. Chem. Int. Ed. Engl. **57**, 551–554 (2018).
- 502 21. Ethylene—Global Market Trajectory and Analytics [https://www.
researchandmarkets.com/reports/354876/ethylene_global_market_trajectory_and_analytics](https://www.researchandmarkets.com/reports/354876/ethylene_global_market_trajectory_and_analytics) (Research and Markets, 2020).
- 503 22. Cheng, T., Xiao, H. & Goddard, W. A. Full atomistic reaction mechanism
504 with kinetics for CO reduction on Cu(100) from ab initio molecular
505 dynamics free-energy calculations at 298 K. *Proc. Natl Acad. Sci. USA* **114**,
506 1795–1800 (2017).
- 507 23. Cheng, T., Xiao, H. & Goddard, W. A. Nature of the active sites for CO
508 reduction on copper nanoparticles; suggestions for optimizing performance.
J. Am. Chem. Soc. **139**, 11642–11645 (2017).
- 509 24. Hori, Y., Takahashi, I., Koga, O. & Hoshi, N. Selective formation of C₂
510 compounds from electrochemical reduction of CO₂ at a series of copper
511 single crystal electrodes. *J. Phys. Chem. B* **106**, 15–17 (2002).
- 512 25. Jin, M. et al. Shape-controlled synthesis of copper nanocrystals in an aqueous
513 solution with glucose as a reducing agent and hexadecylamine as a capping
514 agent. *Angew. Chem. Int. Ed.* **50**, 10560–10564 (2011).
- 515 26. Yang, H. J., He, S. Y. & Tuan, H. Y. Self-seeded growth of five-fold twinned
516 copper nanowires: mechanistic study, characterization, and SERS applications.
Langmuir **30**, 602–610 (2014).
- 517 27. Mandal, L. et al. Investigating the role of copper oxide in electrochemical
518 CO₂ reduction in real time. *ACS Appl. Mater. Inter.* **10**, 8574–8584 (2018).
- 519 28. Baturina, O. A. et al. CO₂ electroreduction to hydrocarbons on
520 carbon-supported Cu nanoparticles. *ACS Catal.* **4**, 3682–3695 (2014).
- 521 29. Droog, J. M. & Schlenter, B. Oxygen electrosorption on copper single crystal
522 electrodes in sodium hydroxide solution. *J. Electroanal. Chem.* **112**,
523 387–390 (1980).
- 524 30. De Chialvo, M. G., Zerbino, J. O., Marchiano, S. L. & Arvia, A. J. Correlation
525 of electrochemical and ellipsometric data in relation to the kinetics and
mechanism of Cu₂O electroformation in alkaline solutions. *J. Appl.
Electrochem.* **16**, 517–526 (1986).
31. Raciti, D. et al. Low-overpotential electroreduction of carbon monoxide using
copper nanowires. *ACS Catal.* **7**, 4467–4472 (2017).
32. Luc, W. et al. Two-dimensional copper nanosheets for electrochemical
reduction of carbon monoxide to acetate. *Nat. Catal.* **1**, 423–430 (2019).
33. De Chialvo, M. G., Marchiano, S. L. & Arvia, A. J. The mechanism of
oxidation of copper in alkaline solutions. *J. Appl. Electrochem.* **14**,
165–175 (1984).
34. Zhang, S., Kang, P. & Meyer, T. J. Nanostructured tin catalysts for selective
electrochemical reduction of carbon dioxide to formate. *J. Am. Chem. Soc.*
136, 1734–1737 (2014).
35. Tian, F. H. & Wang, Z. X. Adsorption of an O atom on the Cu(311) step
defective surface. *J. Phys. Chem. B* **108**, 1392–1395 (2004).
36. Hori, Y., Wakebe, H., Tsukamoto, T. & Koga, O. Adsorption of CO
accompanied with simultaneous charge transfer on copper single crystal
electrodes related with electrochemical reduction of CO₂ to hydrocarbons.
Surf. Sci. **335**, 258–263 (1995).
37. Baricuatro, J. H., Kim, Y. G., Korzeniewski, C. L. & Soriaga, M. P. Seriatim
ECSTM–ECPMIRS of the adsorption of carbon monoxide on Cu(100) in
alkaline solution at CO₂-reduction potentials. *Electrochim. Commun.* **91**,
1–4 (2018).
38. Resasco, J. et al. Promoter effects of alkali metal cations on the
electrochemical reduction of carbon dioxide. *J. Am. Chem. Soc.* **139**,
11277–11287 (2017).
39. Montoya, J. H., Shi, C., Chan, K. & Nørskov, J. K. Theoretical insights into a
CO dimerization mechanism in CO₂ electroreduction. *J. Phys. Chem. Lett.* **6**,
2032–2037 (2015).
40. Seh, Z. W. et al. Combining theory and experiment in electrocatalysis:
insights into materials design. *Science* **13**, 4998 (2017).
41. Yamamoto, S. et al. In situ X-ray photoelectron spectroscopy studies of water
on metals and oxides at ambient conditions. *J. Phys. Condens. Matter* **20**,
184025 (2008).
42. Xiao, H., Cheng, T. & Goddard, W. A. III Atomistic mechanisms underlying
selectivities in C₁ and C₂ products from electrochemical reduction of CO on
Cu(111). *J. Am. Chem. Soc.* **139**, 130–136 (2016).
43. DeWulf, D. W., Jin, T. & Bard, A. J. Electrochemical and surface studies of
carbon dioxide reduction to methane and ethylene at copper electrodes in
aqueous solutions. *J. Electrochem. Soc.* **136**, 1686–1691 (1989).
44. Engelbrecht, A. et al. On the electrochemical CO₂ reduction at copper sheet
electrodes with enhanced long-term stability by pulsed electrolysis.
J. Electrochem. Soc. **165**, J3059–J3068 (2018).
45. Zhu, W. et al. Monodisperse Au nanoparticles for selective electrocatalytic
reduction of CO₂ to C₂O. *J. Am. Chem. Soc.* **135**, 16833–16836 (2013).
46. Kresse, G., Furthmüller, J. & Hafner, J. Theory of the crystal structures of
selenium and tellurium: the effect of generalized-gradient corrections to the
local-density approximation. *Phys. Rev. B* **50**, 13181 (1994).
47. Kresse, G. & Furthmüller, J. Efficiency of ab-initio total energy calculations
for metals and semiconductors using a plane-wave basis set. *Comput. Mater.
Sci.* **6**, 15–50 (1996).
48. Kresse, G. & Furthmüller, J. Efficient iterative schemes for ab initio
total-energy calculations using a plane-wave basis set. *Phys. Rev. B* **54**,
11169 (1996).
49. Perdew, J. P., Burke, K. & Ernzerhof, M. Generalized gradient approximation
made simple. *Phys. Rev. Lett.* **77**, 3865 (1996).
50. Kresse, G. & Joubert, D. From ultrasoft pseudopotentials to the projector
augmented-wave method. *Phys. Rev. B* **59**, 1758 (1999).
51. Grimme, S., Antony, J., Ehrlich, S. & Krieg, H. A consistent and accurate ab
initio parametrization of density functional dispersion correction (DFT-D)
for the 94 elements H–Pu. *J. Chem. Phys.* **132**, 154104 (2010).
52. Matthew, K., Sundaraman, R., Letchworth-Weaver, K., Arias, T. A. &
Hennig, R. G. Implicit solvation model for density-functional study of
nanocrystal surfaces and reaction pathways. *J. Chem. Phys.* **140**, 084106
(2014).
53. Henkelman, G. & Jónsson, H. Improved tangent estimate in the nudged
elastic band method for finding minimum energy paths and saddle point.
J. Chem. Phys. **113**, 9978 (2000).
54. Gao, D. et al. Plasma-activated copper nanocube catalysts for efficient carbon
dioxide electroreduction to hydrocarbons and alcohols. *ACS Nano* **11**,
4825–4831 (2017).
55. Kim, D., Kley, C. S., Li, Y. & Yang, P. Copper nanoparticle ensembles for
selective electroreduction of CO₂ to C₂–C₃ products. *Proc. Natl Acad. Sci.
USA* **114**, 10560–10565 (2017).
56. De Luna, P. et al. Catalyst electro-redistribution controls morphology and
oxidation state for selective carbon dioxide reduction. *Nat. Catal.* **1**,
103–110 (2018).
57. Kim, J. et al. Branched copper oxide nanoparticles induce highly selective
ethylene production by electrochemical carbon dioxide reduction. *J. Am.
Chem. Soc.* **141**, 6986–6994 (2019).

A

B

- 526 58. Jung, H. et al. Electrochemical fragmentation of Cu₂O nanoparticles
 527 enhancing selective C–C coupling from CO₂ reduction reaction. *J. Am. Chem.
 528 Soc.* **141**, 4624–4633 (2019).

Acknowledgements

The TEM work was conducted using the facilities in the Electron Imaging Center at the California NanoSystems Institute at the University of California Los Angles and the Irvine Materials Research Institute at the University of California Irvine. C.C., J.C., X.D. and Y.H. acknowledge support from the Office of Naval Research (ONR) under grant no. N000141712608. S.K., T.C. and W.A.G. were supported by the Joint Center for Artificial Photosynthesis, a DOE Energy Innovation Hub, supported through the Office of Science of the US Department of Energy under Award no. DE-SC0004993. C.L., S.K. and H.M.L. used the Extreme Science and Engineering Discovery Environment (XSEDE), which is supported by National Science Foundation grant no. ACI-1548562. C.L. and H.M.L. were also supported by a National Research Foundation (NRF) of Korea grant funded by the Korean Government (no. NRF-2017R1E1A1A03071049).

Author contributions

C.C. designed and conducted most of the experiments, analysed all the data and prepared the manuscript. S.K., T.C. and W.A.G. performed the density theoretical

calculations and prepared the manuscript. M.X., P.T. and X.P. took SEI and bright-field scanning transmission electron microscopy images. J.C., C.L., H.M.L and X.D. assisted in the experiments and the preparation of the manuscript. Y.H. initiated the study, oversaw the project and wrote the manuscript. All the authors discussed the results and contributed to the manuscript.

Competing interests

The authors declare no competing interests.

Additional information

Supplementary information is available for this paper at <https://doi.org/10.1038/s41929-020-00504-x>.

Correspondence and requests for materials should be addressed to W.A.G. or Y.H.

Reprints and permissions information is available at www.nature.com/reprints.

Publisher's note Springer Nature remains neutral with regard to jurisdictional claims in published maps and institutional affiliations.

This is a U.S. government work and not under copyright protection in the U.S.; foreign copyright protection may apply 2020

QUERY FORM

Nature Catalysis	
Manuscript ID	[Art. Id: 504]
Author	Chungseok Choi

AUTHOR:

The following queries have arisen during the editing of your manuscript. Please answer by making the requisite corrections directly in the e.proofing tool rather than marking them up on the PDF. This will ensure that your corrections are incorporated accurately and that your paper is published as quickly as possible.

Query No.	Nature of Query
Q1:	Please confirm that all of the institutions listed in affiliation 3 are at the same address. If they are not, please split into separate affiliations.
Q2:	Please confirm affiliation 4 is correct.
Q3:	We reserve ‘significant’ and its derivatives to mean statistically significant; for all instances in this paper, please re-word (e.g. ‘important’, ‘notable’, ‘substantial’) or supply a statistical measure such as P value. See the sentence beginning ‘Among the catalysts explored to date ...’ for the first use; in this instance, would ‘substantial’ be OK?
Q4:	As the references were not cited in numerical order (text then figures and tables), they have been renumbered in the order of appearance. Please check this carefully.
Q5:	Please check your article carefully, coordinate with any co-authors and enter all final edits clearly in the eproof, remembering to save frequently. Once corrections are submitted, we cannot routinely make further changes to the article.
Q6:	Note that the eproof should be amended in only one browser window at any one time; otherwise changes will be overwritten.
Q7:	Author surnames have been highlighted. Please check these carefully and adjust if the first name or surname is marked up incorrectly. Note that changes here will affect indexing of your article in public repositories such as PubMed. Also, carefully check the spelling and numbering of all author names and affiliations, and the corresponding email address(es).
Q8:	You cannot alter accepted Supplementary Information files except for critical changes to scientific content. If you do resupply any files, please also provide a brief (but complete) list of changes. If these are not considered scientific changes, any altered Supplementary files will not be used, only the originally accepted version will be published.
Q9:	In the e.proof tool, the numbers for those compounds that will be deposited in PubChem do not appear bold, and the link is not visible. You do not need to amend this, they will appear correctly once published online.
Q10:	In the sentence beginning “They found that the most active ...” could ‘significantly’ be changed to ‘substantially’?
Q11:	Figure 1 was not cited in the original text. Please confirm that the citation at the end of the sentence beginning “Here we report the preparation ...” is OK or move it to a more appropriate place.
Q12:	In the sentence beginning “Significantly, a clear correlation was observed ...” could ‘significantly’ be changed to ‘importantly’?

QUERY FORM

Nature Catalysis	
Manuscript ID	[Art. Id: 504]
Author	Chungseok Choi

AUTHOR:

The following queries have arisen during the editing of your manuscript. Please answer by making the requisite corrections directly in the e.proofing tool rather than marking them up on the PDF. This will ensure that your corrections are incorporated accurately and that your paper is published as quickly as possible.

Query No.	Nature of Query
Q13:	For Fig. 5c, please clarify 'CO+*'.
Q14:	In the sentence beginning "Moreover, the two adjacent molecular CO...", please expand 'STM'.
Q15:	Reference 45 was not originally cited in text. Please confirm that the citation of this reference after the sentence 'under atmospheric pressure' is appropriate or indicate where it should be cited.
Q16:	For equation (1), please clarify subscript 'J'.
Q17:	In equation (10), 'G' represents the gas flow rate, but 'G' is also used for free energy. Please change the former to a different symbol (e.g. ' G_{FR} ').
Q18:	For equation (1), please define ' p '.